Energy & Environmental Science

PAPER

Thermodynamics of energy conversion *via* first order phase transformation in low hysteresis magnetic materials

Yintao Song,[a] Kanwal Preet Bhatti,[ab] Vijay Srivastava,†[a] C. Leighton[b] and Richard D. James*[a]

We investigate the thermodynamics of first order non-ferromagnetic to ferromagnetic phase transformation in low thermal hysteresis alloys with compositions near $Ni_{44}Co_6Mn_{40}Sn_{10}$ as a basis for the study of multiferroic energy conversion. We develop a Gibbs free energy function based on magnetic and calorimetric measurements that accounts for the magnetic behavior and martensitic phase transformation. The model predicts temperature and field induced phase transformations in agreement with experiments. The model is used to analyze a newly discovered method for the direct conversion of heat to electricity [Srivastava *et al.*, *Adv. Energy Mater.*, 2011, **1**, 97], which is suited for the small temperature difference regime, about 10–100 K. Using the model, we explore the efficiency of energy conversion thermodynamic cycles based on this method. We also explore the implications of these predictions for future alloy development. Finally, we relate our simple free energy to more sophisticated theories that account for magnetic domains, demagnetization effects, the crystallography of martensitic phase transformations and twinning.

Broader context

The discovery of new technologies for the generation of electricity without significant greenhouse gas emission is one of the most important environmental imperatives of the 21st century. A recently demonstrated method of converting heat to electricity based on first order phase transformations in multiferroic materials [Srivastava *et al.*, *Adv. Energy Mater.*, 2011, **1**, 97] provides a possible route to this goal, which is potentially applicable to energy conversion using the waste heat from power plants, automobile exhaust systems, and computers, as well as natural solar- and geo-thermal sources. The efficiency of converting heat to electricity, how best to design devices, and how to quantitatively compare this method with other methods of energy conversion rest on thermodynamic arguments. In this paper, we present a thermomagnetic model for this new energy conversion method. Using the model, we explore the efficiency of thermodynamic cycles for energy conversion and the implications of these predictions for future materials development.

1 Introduction

The discovery of new technologies for the generation of electricity without significant greenhouse gas emission is one of the most important environmental imperatives of the 21st century. A recently demonstrated method of converting heat to electricity based on first order phase transformations in multiferroic materials[1,2] provides a possible route to this goal, which is potentially applicable to energy conversion using the waste heat from power plants, automobile exhaust systems, and computers, as well as natural solar- and geo-thermal sources.

[a]Aerospace Engineering and Mechanics, University of Minnesota, Minneapolis, MN 55455, USA. E-mail: james@umn.edu; Tel: +1-612-625-0706

[b]Chemical Engineering and Materials Science, University of Minnesota, Minneapolis, MN 55455, USA

† Current address: GE Global Research Center, 1 Research Circle, Niskayuna, NY 12309, USA.

The general idea makes use of the fact that electromagnetic properties such as magnetization and electric polarization – and many other properties – are sensitive to a change of lattice parameters.[3] Structural phase transformations have an abrupt change of lattice parameters, and therefore can lead to abrupt changes of these properties. Using standard methods of electromagnetic conversion, such as induction and charge separation, the abrupt change of a suitable electromagnetic property can be converted into electricity. The energy obtained in this way arises from a fraction of the latent heat absorbed. An attractive feature of this method is the elimination of the generator: the heat is converted *directly* to electricity by the material. What fraction of the latent heat is converted to electricity, how best to design the device, and how to quantitatively compare this method with other methods of energy conversion rest on thermodynamic arguments.

The purpose of this paper is to present a thermodynamic model for energy conversion using a first order phase

This journal is © The Royal Society of Chemistry 2013

Energy Environ. Sci., 2013, **6**, 1315–1327 | **1315**

transformation with an abruptly changing magnetization. We evaluate explicitly the thermodynamic functions in the theory for the alloy $Ni_{44}Co_6Mn_{40}Sn_{10}$, which has been subject to a detailed characterization study by calorimetry, wide angle X-ray diffraction, SQUID magnetometry and small angle neutron scattering.[4] (The alloy used in the energy conversion demonstration[2] was the nearby alloy $Ni_{45}Co_5Mn_{40}Sn_{10}$.) This off-stoichiometric Heusler alloy undergoes a cubic (space group $Fm\bar{3}m$) to monoclinic (space group $P2_1$, 5M-modulated) martensitic phase transformation at about 390 K, with a sudden change of magnetization. The evidence[4] suggests the martensite is antiferromagnetic with a small fraction of nanoscale spin clusters, which may be retained austenite. The austenite phase of $Ni_{44}Co_6Mn_{40}Sn_{10}$ is ferromagnetic with a magnetization of 8×10^5 A m^{-1} (800 emu cm^{-3}) at 4 T near the transformation temperature. It is fascinating to add that the nearby alloy $Ni_{45}Co_5Mn_{40}Sn_{10}$ has a measured magnetization in austenite of 1.17×10^6 A m^{-1}, but either an increase or a decrease of Co by 1%, substituted for Ni, leads to a significant drop of magnetization. This extreme sensitivity of magnetization to ±1% changes of composition remains unexplained.

As explained in detail elsewhere[1,4] the alloys with composition near $Ni_{45}Co_5Mn_{40}Sn_{10}$ were found by combining the search for an abrupt change of magnetization, beginning from earlier work of Kainuma[5–7] and others,[1,8–10] with a systematic procedure to lower hysteresis by improving the compatibility between phases. This involves the tuning of lattice parameters by changing composition so that a perfect unstressed interface is possible between the austenite and a single variant of martensite.[3,11–13] The technical condition for this is $\lambda_2 = 1$, where λ_2 is the middle eigenvalue of the transformation stretch matrix.[3,11,12] Having $\lambda_2 = 1$ does not contradict an otherwise large change of lattice parameters, i.e., the other eigenvalues of the transformation stretch matrix can still remain far away from 1, so the aforementioned abrupt change of lattice parameters is still possible. This elimination of the usual stressed transition layer between austenite and martensite has been shown to drastically lower the hysteresis of the transformation and also to significantly reduce the migration of the transformation temperature of the alloy under repeated cycling,[14,15] a primary indicator of degradation. $Ni_{45}Co_5Mn_{40}Sn_{10}$ has a measured value $\lambda_2 = 1.0042$ and a thermal hysteresis of about 6 K. Both lowered hysteresis and a high degree of reversibility of the phase transformation are important in energy conversion applications.
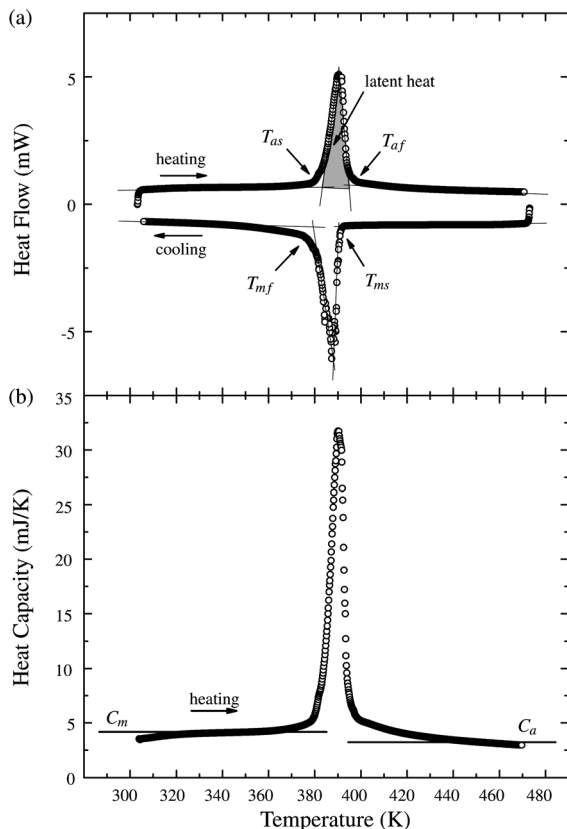
The model can also be used to analyze magnetic refrigeration based on magnetocaloric effect.[16,17] Materials showing this effect can use changes in magnetic field to move heat from hot to cold regions. In fact, our prototype material $Ni_{44}Co_6Mn_{40}Sn_{10}$ is close to the Ni–Mn–Sn alloy system which has been identified to have "inverse magnetocaloric effect".[8] The magnetic refrigeration near room temperature is enabled by the discovery of a so-called giant magnetocaloric effect,[18] which typically occurs in materials having a first order martensitic phase transformation.[19,20] The magnetic ordering also changes abruptly during such transformations. It can change from strong ferromagnetic martensite to weak ferromagnetic austenite phase,[18,19]

weak ferromagnetic martensite to strong ferromagnetic austenite,[8] or antiferromagnetic martensite to ferromagnetic austenite[20,21] as in our prototype alloy. Some magnetocaloric alloys also have low hysteresis,[22] although the connection with the alloy development strategy, $\lambda_2 \to 1$, is unknown. Since the thermodynamic cycles of a refrigerator and a heat engine working at the same temperature difference are identical except for the signs of the net work done and heat absorbed, our explicit free energy and our analysis of energy conversion cycles can be easily adopted to magnetic refrigerators.

The organization of the paper is as follows. After reviewing experimental methods in Section 2, we describe, in Section 8, how the simple free energy function used in the paper is related to more general thermodynamic/micromagnetic models that account for magnetic domains, twinning and martensitic phase transformation. This comparison sharply defines the domain of application and transferability of our model. Section 3 describes our procedure for determining the free energy based on magnetic and calorimetric measurements: a simple spin-1 Brillouin function is found to work remarkably well. This section fully accounts for phase transformation. Section 4 compares the predictions of this free energy with further experimental observations (not used in the evaluation of the free energy) involving field and temperature induced phase transformations. In Section 5, we study several thermodynamic (thermomagnetic) cycles that are possible according to the theory and which are interesting from the point of view of the direct conversion of heat to electricity. We relate these thermomagnetic cycles to the electric work output of a proposed device utilizing this method of energy conversion in Section 6. Finally, in Section 7, we summarize the main conclusions.

2 Experimental section

The active material for the characterizations was obtained from a polycrystalline ingot (3 g) of $Ni_{44}Co_6Mn_{40}Sn_{10}$ prepared by arc melting the elemental materials Ni (99.999%), Mn (99.98%), Co (99.99%) and Sn (99.99%) under positive pressure of argon. The arc melting furnace was purged three times and a Ti getter was melted prior to melting each sample. To promote homogeneity, the ingot was melted and turned over six times. Conversion from A m^2 kg^{-1} to A m^{-1} was done with a density 8.0 g cm^{-3}. All samples were weighed before and after melting and lost less than 1% by mass. The resulting buttons were homogenized in an evacuated and sealed quartz tube at 900 °C for 24 h, and quenched in room-temperature water. Differential scanning calorimetry (DSC) measurements were done on a Thermal Analyst, calibrated with indium, at a heating and cooling rate of ±10 K min^{-1} between 225 and 475 K. For the DSC measurements, each sample was thinned and finely polished to ensure good thermal contact with the pan. For polycrystalline $Ni_{44}Co_6Mn_{40}Sn_{10}$ (Fig. 1) such measurements reveal $T_{ms} = 398$ K, $T_{mf} = 388$ K, $T_{as} = 382$ K, and $T_{af} = 392$ K, where T_{ms}, T_{mf}, T_{as}, and T_{af} are the martensite start, martensite finish, austenite start, and austenite finish temperatures using the standard parameterization of martensitic phase transformation temperatures. Magnetometry was done in a Quantum Design SQUID

1316 | Energy Environ. Sci., 2013, 6, 1315–1327

This journal is © The Royal Society of Chemistry 2013

Fig. 1 (a) Heat flow and (b) heat capacity *vs.* temperature measured by DSC at heating/cooling rate of 10 K min^{-1}. T_{ms}, T_{mf}, T_{as}, and T_{af} are the martensite start/finish and austenite start/finish temperatures, respectively. The latent heat computed from the graph is $L = 13.17$ J g^{-1}. $C_a = 3.65$ mJ K^{-1} and $C_m = 3.90$ mJ K^{-1} are the average heat capacities for austenite and martensite single phases, respectively.

magnetometer from 5 to 600 K, in applied magnetic fields from 0.001 to 7 T. For low-field measurements the remnant field profile in the superconducting magnet was measured, and the field at the sample nulled to $\ll 1 \times 10^{-4}$ T. The magnetic properties of Ni$_{44}$Co$_6$Mn$_{40}$Sn$_{10}$ used in the present study are taken from ref. 4.

3 Free energy function

We now build up a thermodynamic model to describe the first order phase transformation in materials having different magnetic properties in the two phases. According to classical equilibrium thermodynamics, the Gibbs free energy ψ as a function of external magnetic field H and temperature T in a *single phase material* satisfies the Maxwell relations

$$\frac{\partial \psi(H,T)}{\partial H} = -\mu_0 M, \quad \frac{\partial \psi(H,T)}{\partial T} = -S. \quad (1)$$

Integrating the first relation, we have

$$\psi(H,T) = -\mu_0 \int_0^H M(h,T)\mathrm{d}h + f(T), \quad (2)$$

where $f(T)$ is the field-independent component of the free energy, and $M(H, T)$ is the magnetization as a function of external field and temperature. The latter can be obtained from single-phase M–H and M–T measurements reported in the following sections, where the exact method of interpolation is also provided. Based on eqn (2), we can express entropy and heat capacity as

$$S(H,T) = -\mu_0 \int_0^H \frac{\partial M(h,T)}{\partial T}\mathrm{d}h + \frac{\mathrm{d}f(T)}{\mathrm{d}T}, \quad (3a)$$

$$C(H,T) = T\frac{\partial S(H,T)}{\partial T}. \quad (3b)$$

When no field is applied, $\psi(H, T)$ reduces to $f(T)$, and the heat capacity is simply $C(0, T) = T(\mathrm{d}^2 f/\mathrm{d}T^2)$. Based on DSC data of the alloys of interest (Fig. 1), we treat the heat capacity of each phase as a constant, denoted by C_m and C_a for martensite and austenite phases, respectively. (Throughout this paper, we use subscripts m or a to denote the thermodynamic functions in martensite or austenite single phase, respectively. Functions without subscripts pertain to the state of the whole specimen, including two-phase mixtures.) The entropy of each phase at zero field then can be obtained by integrating eqn (3b) over the second argument at $H = 0$ from T_0 to T.

$$S_m(0,T) = C_m\ln(T/T_0) + C_1, \quad (4a)$$

$$S_a(0,T) = C_a\ln(T/T_0) + C_2, \quad (4b)$$

where T_0 is the zero-field transformation temperature given by the DSC measurement, and the difference of integration constants $C_1 - C_2$ is evaluated from
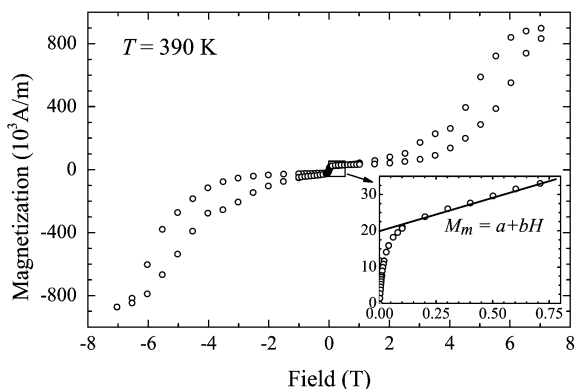
$$[S_a(0,T_0) - S_m(0,T_0)]T_0 = L, \quad (5)$$

using the measured zero-field latent heat per unit volume, L. By basic thermodynamic principles excluding the equivocal third law of thermodynamics, only the difference $C_1 - C_2$ has physical meaning in a temperature range bounded away from $T = 0$ K. Without loss of generality, we therefore choose $C_1 = 0$ and $C_2 = L/T_0 - \Delta C$, $\Delta C = C_a - C_m$. Then using eqn (3a), we have the field-independent components of free energy functions

$$f_m(T) = -C_m[T_0 - T + T\ln(T/T_0)] + C_3, \quad (6a)$$

$$f_a(T) = -C_a[T_0 - T + T\ln(T/T_0)] - (L/T_0 - \Delta C)T + C_4. \quad (6b)$$

$C_3 = -(L - \Delta C T_0)$ and $C_4 = 0$ are determined by the condition $f_a(T_0) = f_m(T_0)$. Substituting f's back into eqn (2) leads to the complete free energy functions, once the magnetization function $M(H, T)$ is obtained. The M–H curve of the alloy at 390 K is plotted in Fig. 2. In the figure, we see that the M–H curve can be divided into three regions: low field (<0.25 T), intermediate field (between 0.25 and 2 T), and high field (>2 T). In the low field region, a small fraction of the specimen that is ferromagnetic quickly saturates. After saturating the ferromagnetic component, in the intermediate field region, the linear response due to the antiferromagnetic component dominates. Finally, we

This journal is © The Royal Society of Chemistry 2013

Energy Environ. Sci., 2013, **6**, 1315–1327 | **1317**

Fig. 2 Fitting of M–H curve for martensite near the transformation temperature. The fitting parameters obtained from the graph are a = 19 748 A m^{-1} and b = 19.3183.

observe a field induced phase transformation in the high field region. Since the field used in the energy conversion is usually in the intermediate region, for the martensite phase, we use an affine function, $M_m(H) = a + bH$, to fit its M–H response, with two temperature-independent parameters a and b, as shown in Fig. 2. The total free energy of martensite phase is then $\psi_m(H, T) = \mu_0(aH + bH^2/2) + f_m(T)$.

The difference between the linear fitting and the nonlinear data at low fields may contribute a small additive constant ($\sim 10^{-6}$ J cm^{-3}) to the free energy at intermediate fields after integration. As explained in Section 4, the temperatures T_{as} and T_{af} computed from eqn (11) are characterized by two constant differences ($\Delta\Psi_s$ and $\Delta\Psi_f$ in Section 4) between the Gibbs free energies of austenite and martensite single phases. The constant introduced here by the discrepancy between data and linear fitting in the low field region can be absorbed into those two fitting parameters. We drop it for simplicity.

For the austenite phase, we use the Weiss molecular field theory to derive the magnetization function, $M_a(H, T)$. Although it is considered more accurate to use the Heisenberg Hamiltonian to describe the interactions between atomic moments, the Weiss molecular field theory matches experiments very well within the range of temperature and field of interest, as shown below in Fig. 3. Furthermore, the simplicity of this model and its capability of reproducing the measured effect of field on transformation temperature is appealing. In molecular field theory, each atom (or molecule in Weiss' terminology, or formula unit in our calculation) in the crystal is assumed to have a magnetic moment, $\mu_m\boldsymbol{J}$, where μ_m is the magnitude and $\boldsymbol{J}$ is the direction of the moment. The magnetization is then $M = N_v\mu_m \langle J \rangle$, where N_v is the number of spins per unit volume. In our fitting, we found two spin sites per formula unit worked well. $\langle J \rangle$ is the mean value of the projection of $\boldsymbol{J}$ along a certain direction, usually the direction of the external field. Weiss assumed that the interaction between an atom and all the others can be described as an effective internal magnetic field, called the *molecular field*, which is proportional to the magnetization, $\mu_0 H_m = \gamma M$, where γ is the *molecular field constant*. We use the spin-1 Brillouin function, *i.e.* assuming $J = 1$, to compute the mean value of atomic moments
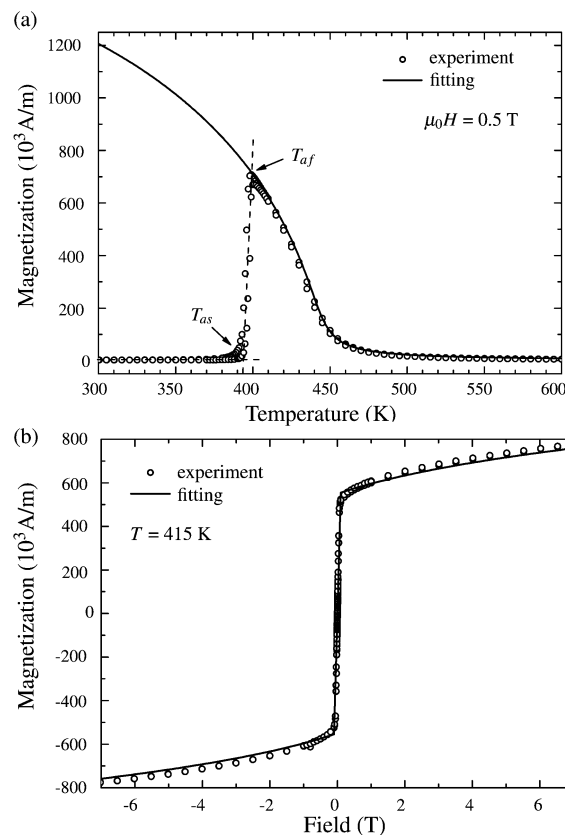
Fig. 3 Magnetization of austenite phase as a function of (a) temperature and (b) field calculated by Weiss molecular field theory. Open circles are experimental data for both heating and cooling,[4] solid lines are fitted by Brillouin function with μ_m = 4.2 μ_B, which is the same as 8.4 μ_B/f.u., and the molecular field constant is γ = 1573.55 T m A^{-1}. The result shows excellent agreement with experimental data in both M_a *vs.* T at fixed H and M_a *vs.* H at fixed T curves. The formula unit used here is Ni$_{1.76}$Co$_{0.24}$Mn$_{1.60}$Sn$_{0.40}$. $M_0 = N_v\mu_m$ is the calculated saturation magnetization at T = 0 K.

$$\langle J \rangle = B_1\left[\frac{\mu_m(\gamma N_v\mu_m\langle J \rangle + \mu_0 H)}{k_B T}\right], \qquad (7)$$

where k_B is Boltzmann constant and $B_j(a)$ is the jth Brillouin function

$$B_j(z) = \frac{2j+1}{2j}\coth\left(\frac{2j+1}{2j}z\right) - \frac{1}{2j}\coth\left(\frac{z}{2j}\right). \qquad (8)$$

The choice $J = 1$ is reasonable (see ref. 23) and provides a good fit, but is not supported by knowledge of the detailed magnetic ordering of Ni$_{44}$Co$_6$Mn$_{40}$Sn$_{10}$. As far as we know, the data needed for a quantitative calculation of J for austenite is unavailable for this alloy.

Eqn (7) gives the magnetization in austenite phase as a function of temperature and field through the relation $M = N_v\mu_m \langle J \rangle$. When $H = 0$, it reduces to the spontaneous magnetization as a function of temperature only. The temperature where this spontaneous magnetization vanishes is the Curie temperature. The molecular field constant γ which fits best the data and which is used in following calculation gives a Curie temperature of 439 K. The M–T curve of the same material measured at a low field (10^4 A m^{-1}) shows that the Curie

1318 | *Energy Environ. Sci.*, 2013, **6**, 1315–1327

This journal is © The Royal Society of Chemistry 2013

Table 1 Parameters used in the fitting of austenite magnetization function, $M_a(H, T)$, in $Ni_{44}Co_6Mn_{40}Sn_{10}$. Heat capacities C_m and C_a (J cm^{-3} K^{-1}), and the latent heat L (J cm^{-3}) are obtained from the DSC measurement (Fig. 1). The atomic moment μ_m (μ_B) and the molecular field constant γ (T m A^{-1}) for the austenite phase (Fig. 3), and coefficients a (A m^{-1}) and b (dimensionless) for the martensite phase (Fig. 2), are fit to the Curie temperature and M–H, M–T curves from the SQUID data

C_m	C_a	L	μ_m	γ	a	b
2.40	2.22	105.36	4.2	1573.55	19 748	19.3183

temperature is about 425 K.[4] The discrepancy between fitted and measured values of the Curie temperature suggests that the magnetic property of this material cannot be fully explained by such a single magnetic sublattice $J = 1$ molecular field approximation. The reasons include the interaction between multiple magnetic sublattices (Ni/Co, Mn$_1$, Mn$_2$)[24] and the spatial disordering of species in such an off-stoichiometric alloy.[24] In a nutshell, getting a more accurate M–H response in the region where no magnetic measurement of austenite is available, *i.e.* below the transformation temperature, is rather difficult. However, for the purpose of studying small shifts in transformation temperature, as we do in the rest of this paper, this simple fitting model is sufficient. The fitting of austenite magnetization in $Ni_{44}Co_6Mn_{40}Sn_{10}$ is shown in Fig. 3. The parameters used in the fitting are listed in Table 1.

Overall, the fitting of this data to the function $M_a(H, T)$ is excellent. The small discrepancy occurring at low field (<0.1 T) is likely to be a result of complex domain interactions arising from the competition of demagnetization and anisotropy energies. The fact that the saturation magnetization at 0 K is much larger than the high field magnetization on the M_a–H curve in Fig. 3b is because 415 K is very close to the Curie temperature,[25] which is about 425 K for this alloy.

In summary, the Gibbs free energy used in the rest of this paper is defined explicitly by

$$\psi(H, T) = -\mu_0 \int_0^H M(h, T)\mathrm{d}h + f(T), \qquad (9)$$

where $M = M_a(H, T) = N_v\mu_m\langle J\rangle$ for the austenite phase, with $\langle J\rangle$ given by eqn (7) and (8) evaluated with μ_m given in Table 1, $M_m(H) = a + bH$ for the martensite phase (a, b in Table 1), and f for martensite and austenite, respectively, given by eqn (6) (C_a, C_m, L in Table 1).

4 Temperature and field induced phase transformation

The transformation temperature $T_M = T_M(H)$ as a function of the field H is defined as the temperature where the Gibbs free energy functions of two phases are the same at the given field (Fig. 4a), *i.e.*,

$$\psi_a(H, T_M(H)) = \psi_m(H, T_M(H)). \qquad (10)$$

The variation of T_M with changes of H defines the effect of field on transformation temperature, which is usually
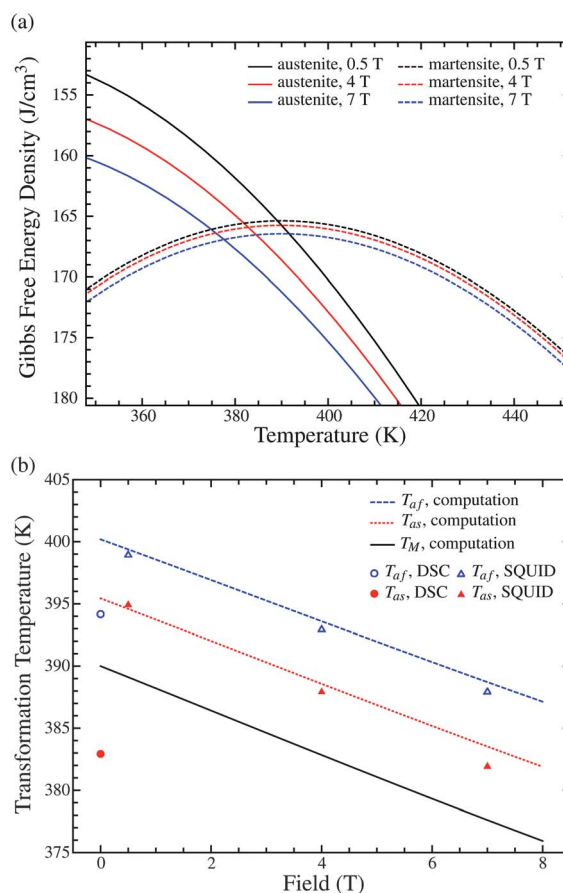
Fig. 4 (a) Gibbs free energy of both phases expressed as eqn (2) and (b) the transformation temperature as a function of field computed from eqn (10). The simulation of T_{as} and T_{af} are computed from eqn (11) with the energy barriers $\Delta\psi_s$ and $\Delta\psi_f$ as two fitting parameters. The method of obtaining T_{as} and T_{af} from M–T curves is shown in Fig. 3a. For the alloy $Ni_{44}Co_6Mn_{40}Sn_{10}$, $\Delta\psi_s = -2.3$ J cm^{-3} and $\Delta\psi_f = -4.3$ J cm^{-3}.

quantified by differentiating eqn (10) with respect to H and using eqn (1). The result is a version of the *Clausius–Clapeyron relation* appropriate to magnetic field induced transformation.

Note that the Gibbs free energies in Fig. 4a are not monotonically decreasing, which means that the entropy is not positive at all temperatures. This can be fixed by adding an affine function of temperature $c_1T + c_2$ to the Gibbs free energy, which preserves all the results of the paper. In our case c_1 could be chosen to make the entropy positive. We could in fact adjust c_1 and c_2 to satisfy the classical version of the third law of thermodynamics. Since this law is controversial and since the low temperature behavior of $Ni_{44}Co_6Mn_{40}Sn_{10}$ involves a number of unusual effects such as exchange bias, which we have not modeled, we did not do this. The entropy does increase as the temperature increases, which is shown as the concavity of Gibbs free energies.

In order to initiate the transformation from martensite to austenite, the critical temperature T_{as} must be slightly higher than the computed T_M, due to the existence of an energy barrier between two equal depth energy wells at T_M. We denote such an energy barrier $\Delta\psi_s$. A similar concept is applied to the

temperature T_{af} with a different constant $\Delta\psi_f$. Thus in the model, the temperature T_{as} and T_{af} are determined through

$$\psi_a(H, T_{as}) - \psi_m(H, T_{as}) = \Delta\psi_s, \qquad (11a)$$

$$\psi_a(H, T_{af}) - \psi_m(H, T_{af}) = \Delta\psi_f. \qquad (11b)$$

The constants on the right hand sides are chosen to give agreement with the measured transformation temperature at 0.5 T. Then it is seen from Fig. 4b that the predicted variation of transformation temperature with magnetic field matches experimental data quite well for fields in the range $0 < \mu_0 H < 8$ T in $Ni_{44}Co_6Mn_{40}Sn_{10}$. One remark here is that the zero-field experimental data is obtained from the DSC measurement, while the measured austenite start and finish temperatures, denoted by T_{as} and T_{af} respectively, are interpolated from SQUID data. The measurements from these two methods are slightly different from each other.

By the inspection of the M–T curves in Fig. 5a, the transition between two phases is abrupt but not perfectly sharp. An exact quantitative model of this phenomenon would require a detailed study of the mechanism of nucleation,[4] and could also involve an assessment of demagnetization and rate effects. However, simple rate-independent models[23] have been

successfully used for the quasi-static regime as in our case, and we adopt this simple approach. Therefore, following Maat et al. in ref. 23, we approximate $\partial M(H, T)/\partial T$ during the phase transformation by a Gaussian. Specifically, we assume that the average magnetization of the specimen is given by

$$M(H, T) = [1 - \chi(\bar{A}, \Delta A, T)]M_m(H) + \chi(\bar{A}, \Delta A, T)M_a(H, T), \quad (12)$$

where $\bar{A} = [T_{as}(H) + T_{af}(H)]/2$, $\Delta A = T_{af}(H) - T_{as}(H)$, and

$$\chi(x_c, \Delta, x) = \frac{1}{2}\left[1 + \text{erf}\left(\frac{x - x_c}{\sqrt{2\Delta^2}}\right)\right] \qquad (13)$$

is the cumulative distribution function of the Gaussian, which might be interpreted as the volume fraction of austenite.

The calculated temperature and field induced phase transformations compared with experimental data are shown in Fig. 5. The primary features of these curves are captured reasonably well by our method.

5 Thermodynamic cycles

A thermodynamic cycle consists of a sequence of thermodynamic processes (often quasi-static) of a system in which the state variables return to their original values after one period. During the cycle, heat and mechanical, electrical or magnetic work can be transferred between the system and the environment. Thermodynamic cycles are useful for analyzing energy conversion systems.

The analog of the traditional P–V diagram in the present case is the H–M diagram, which is Fig. 5b with the axes interchanged. As in the traditional case when phase transformation is present, a subset of the T–S or H–M diagrams may consist of a *mixed phase region*. This region is defined as the set of values of the state variables for which both phases minimize the Gibbs free energy and therefore the state variables for the individual phases necessarily give the same Gibbs free energy. In the mixed phase region an additional state variable, the volume fraction $0 < \chi < 1$ of, say, austenite, is introduced. In our case the values of the state variables $T, H, S_a, S_m, M_a, M_m, \chi$ in the mixed phase region are determined by the equilibrium conditions (1), the conditions that M and S are extensive variables, $M = (1 - \chi)M_m + \chi M_a$, $S = (1 - \chi)S_m + \chi S_a$, and the condition that the Gibbs free energy functions of the two phases are the same, i.e., $\psi_a(H, T) = \psi_m(H, T)$. The values of M_a, M_m are the corresponding equiminimizers of the Gibbs free energy. If these conditions cannot be satisfied, or the domains of the free energies φ or ψ exclude certain values of the state variables, then these regions must be excluded from the thermodynamic diagrams. The latter is also important for the evaluation of energy conversion devices.

The measured value $\lambda_2 = 1.0042$ in $Ni_{45}Co_5Mn_{40}Sn_{10}$ corresponds to a thermal hysteresis of 6 K (ref. 1) which is quite low. In similar systems, by carefully tuning λ_2 even closer to 1, thermal hysteresis has been reproducibly tuned to less than 1 K in films produced by combinatorial synthesis methods,[14] and between 2 and 3 K in arc-melted buttons.[15] Similar results have been achieved in a variety of materials, including both metals and oxides.[26,27] We assume that these procedures extend to the
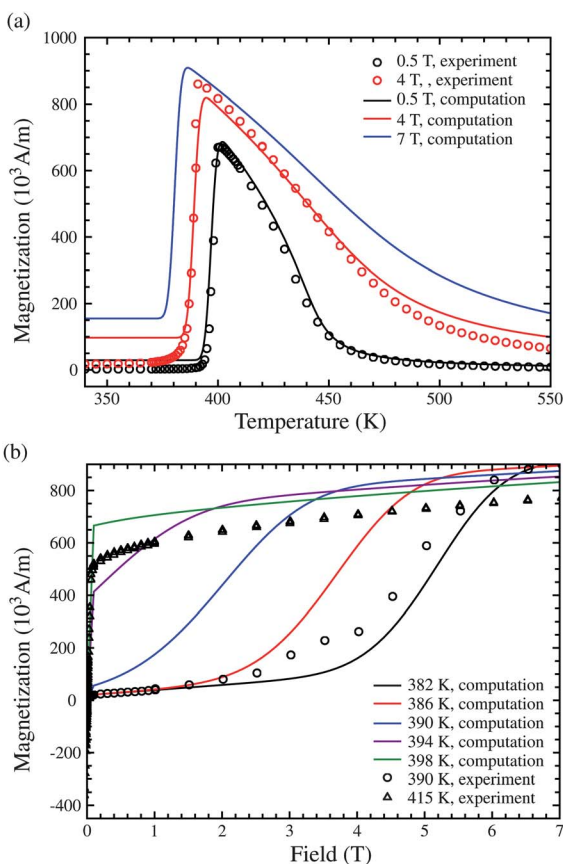
Fig. 5 Total magnetization of the whole specimen (a) varies with temperature at fixed field, and (b) with field at fixed temperature. Experimental data in these plots were measured for heating. Full datasets including heating and cooling refer to ref. 4.

1320 | *Energy Environ. Sci.*, 2013, **6**, 1315–1327

This journal is © The Royal Society of Chemistry 2013

kinds of materials discussed here so that the (already low) hysteresis is even further lowered, so we neglect the losses due to hysteresis in the arguments below.

We now describe the thermodynamic diagrams based on the specific free energy evaluated above for $Ni_{44}Co_6Mn_{40}Sn_{10}$. The most useful is the T–S diagram shown in Fig. 6, because the area of a loop in the T–S diagram is the net work output, due to the first law of thermodynamics. By direct calculation based on the Gibbs free energy determined in Section 3, the mixed phase region is represented in this diagram by the region between the dotted curved on the left, corresponding to martensite, and the series of dashed curves on the right for austenite. There are several curves on the right due to the effect of magnetic field H on transformation temperature, $i.e.$, the mixed phase region depends on both independent variables H and T. Overall efficiency is of course affected by how this is recovered, either by induction or some other process. We defer a discussion of the latter to Section 6.

The mixed phase region, between the dotted and dashed lines in Fig. 6, is the most interesting region for energy conversion, because in this region the latent heat can utilized. By definition, the efficiency η of a cycle is W/Q^+, where W is the net work done and Q^+ is the heat absorbed. That is, if the cycle is parameterized by $(T(t), S(t))$, $0 \leq t < t_1$,

$$Q^+ = \int_{\mathcal{T}^+} T(t)\dot{S}(t)\mathrm{d}t, \tag{14}$$

where $\mathcal{T}^+$ is the set of times in the interval $[0, t_1]$ for which $\dot{S}(t) > 0$. Carnot cycles are by definition rectangles in the T–S diagram, and these give maximum efficiency $\eta_{\text{Carnot}} = 1 - T_{\min}/T_{\max}$ among all cycles operating between temperatures $T_{\min} < T_{\max}$, by a classical argument. As one can see from Fig. 6, the thermomagnetic model given in Section 8–4 admits Carnot cycles of reasonable size in the mixed phase region. Note that Carnot cycles are also possible in the single phase austenite
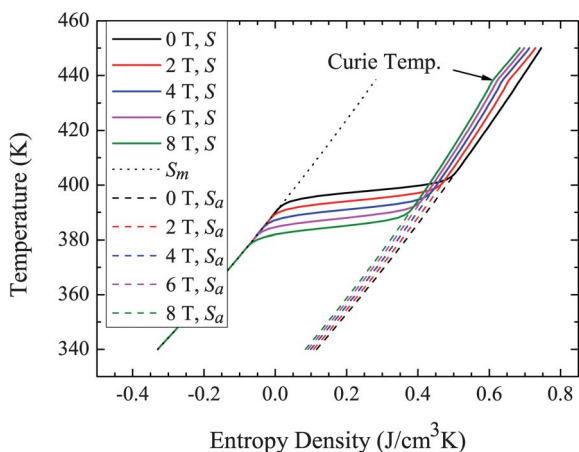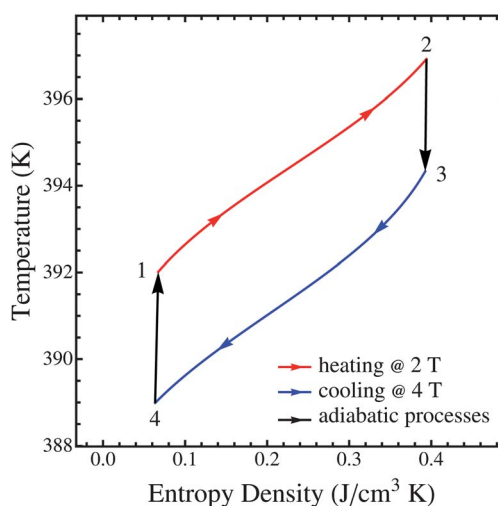
region – the upper right in Fig. 6 – although they are so small as to be impractical in our example and also entail exceptionally large changes of the external field over small temperature intervals.

Observe that the predicted constant field lines in the mixed phase region shown in Fig. 6 are not perfectly horizontal. Hence Carnot cycles in the mixed phase region require a changing field on the isothermal segments. It may be possible to design devices with this feature, but a simpler approach is to consider cycles having two adiabatic segments alternating with two constant field segments. The resulting cycle is the thermomagnetic analog of the Rankine cycle, and we therefore term this a *thermomagnetic Rankine cycle*. Such a thermomagnetic Rankine cycle is illustrated in Fig. 7. Its efficiency can be computed by direct calculation of Q^+ and W using the first law of thermodynamics. Geometrically, the efficiency is the ratio between the area enclosed by the loop $1 \rightarrow 2 \rightarrow 3 \rightarrow 4 \rightarrow 1$ and that below the curve $1 \rightarrow 2 \rightarrow 3$.

Another classical cycle, used widely in jet engines, is the air-standard Ericsson cycle. It also can be adapted to the case of phase transformation and thermomagnetic materials, so we term the resulting cycle the *thermomagnetic Ericsson cycle*. The thermomagnetic Ericsson cycle contains two isothermal segments alternating with two constant field segments. It is defined as follows.

1. Process $1 \rightarrow 2$: heating at constant field. The working material, $Ni_{44}Co_6Mn_{40}Sn_{10}$ in our example, is initially placed in the field $H_{\min}$ at the temperature $T_{\min}$, denoted as "1" in Fig. 8. It is heated to $T_{\max}$ at the constant field. Ideally, the heat for this purpose solely comes from process $3 \rightarrow 4$.

Fig. 6 Constant field curves in T–S diagram. The dotted line is the entropy of martensite single phase, which is field independent. The dashed lines are the entropy of austenite single phase at different fields, and solid lines are the entropy of the whole specimen containing both phases.

Fig. 7 A thermomagnetic Rankine cycle. This cycle differs from the thermomagnetic Ericsson cycle by replacing two isothermal processes by adiabatic processes. Two fields are still $H_{\min} = H_0 - \Delta H$ and $H_{\max} = H_0 + \Delta H$, while four temperatures are chosen to be $T_1 = T_{\text{as}}(H_{\max})$ and $T_2 = T_{\max} = T_{\text{af}}(H_{\min})$, according to eqn (11), T_3 and $T_4 = T_{\min}$ are the solutions to $S(H_{\min}, T_2) = S(H_{\max}, T_3)$ and $S(H_{\min}, T_1) = S(H_{\max}, T_4)$ respectively. In this drawing, we use $\mu_0 H_0 = 3$ T and $\mu_0 \Delta H = 1$ T. The efficiency is given by the ratio between the area enclosed by the loop $1 \rightarrow 2 \rightarrow 3 \rightarrow 4 \rightarrow 1$ and that below the curve $1 \rightarrow 2 \rightarrow 3$.
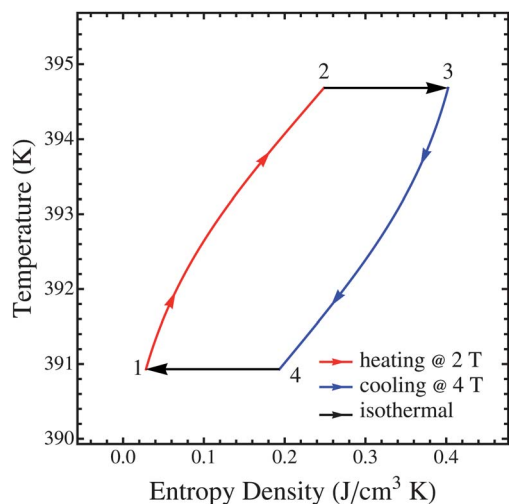
Fig. 8 A thermomagnetic Ericsson cycle. The cycle contains a constant field heating (red arrowed line) from T_{min} to T_{max} at H_{min}, a constant field cooling (blue arrowed line) from T_{max} to T_{min} at H_{max}, and two isothermal processes (black arrowed lines) switching between two fields isothermally. Two fields are given by $H_{min} = H_0 - \Delta H$ and $H_{max} = H_0 + \Delta H$, while two working temperatures are $T_{max,min} = [T_{as}(H_{min}) + T_{af}(H_{max})]/2 \pm \delta T$, according to eqn (11), and δT is chosen to satisfy eqn (15). In this drawing, we use $\mu_0 H_0 = 3$ T and $\mu_0 \Delta H = 1$ T. The efficiency is given by the ratio between the area enclosed by the loop $1 \to 2 \to 3 \to 4 \to 1$ and that below the curve $1 \to 2 \to 3$.

2. Process $2 \to 3$: isothermal magnetization. The field is increased to H_{max} without change of temperature. Heat is absorbed during this process.

3. Process $3 \to 4$: cooling at constant field. The working material is actively cooled to the temperature T_{min} at the constant field H_{max}. Heat is emitted during this process. Ideally, this heat is completely used to heat the material in the process $1 \to 2$.

4. Process $4 \to 1$: isothermal demagnetization. The field is decreased to H_{min} isothermally, returning the working material to state 1.

An attractive feature of the thermomagnetic Ericsson cycle, as in the ordinary Ericsson cycle, is that if dissipative processes are neglected, the Carnot efficiency is achieved. This is achieved by using, and only using, the heat emitted in process $3 \to 4$ as the supply for the heating process $1 \to 2$, so that the heat-exchange with the external environment is no longer required during either process $1 \to 2$ or $3 \to 4$. This technique is called "regeneration". The thermomagnetic model given in Sections 3 and 4 (also in appendix) admits these ideal thermomagnetic Ericsson cycles. To see this, the material properties have to be such that during the constant field heating $1 \to 2$ the heat absorbed has to be equal to the heat emitted during $3 \to 4$, and, at the same time, these segments must begin and end on the same isothermal segments. This is possible according to the following argument. Referring to Fig. 8, consider parameterizing the constant field segments $1 \to 2$ and $4 \to 3$ by functions $S_{12}(T)$ and $S_{43}(T)$ using T as a parameter. These sigmoidal curves have the property that there is a temperature T_s such that $dS_{12}/dT < dS_{43}/dT$ for $T < T_s$ and $dS_{12}/dT > dS_{43}/dT$ for $T > T_s$. Thus, by the intermediate value theorem, there are values $T_{min} < T_s < T_{max}$ such that

$$\int_{T_{min}}^{T_{max}} T \frac{dS_{12}}{dT} dT = \int_{T_{min}}^{T_{max}} T \frac{dS_{43}}{dT} dT. \tag{15}$$

This is the equality of heats in $1 \to 2$ and $4 \to 3$. In fact, it is seen that over a broad range of temperatures in the mixed phase region, $T_{min} < T_s$ can be assigned and then T_{max} can be determined such that eqn (15) holds. Fig. 8 shows an example of a thermomagnetic Ericsson cycle where eqn (15) has been satisfied by a simple numerical procedure.

There are numerous potential device designs utilizing back-to-back plates of active material, together with suitable flux paths that could be used to approximate the conditions of either thermomagnetic Carnot or Ericsson cycles. The switching of the field can also be integrated as part of the device. For example, in the demonstration[2] the current produced in the surrounding coil exerted a back-field on the specimen, which had the effect of altering the field.

The maximum efficiency for conventional thermoelectric materials is given by the formula[28,29]
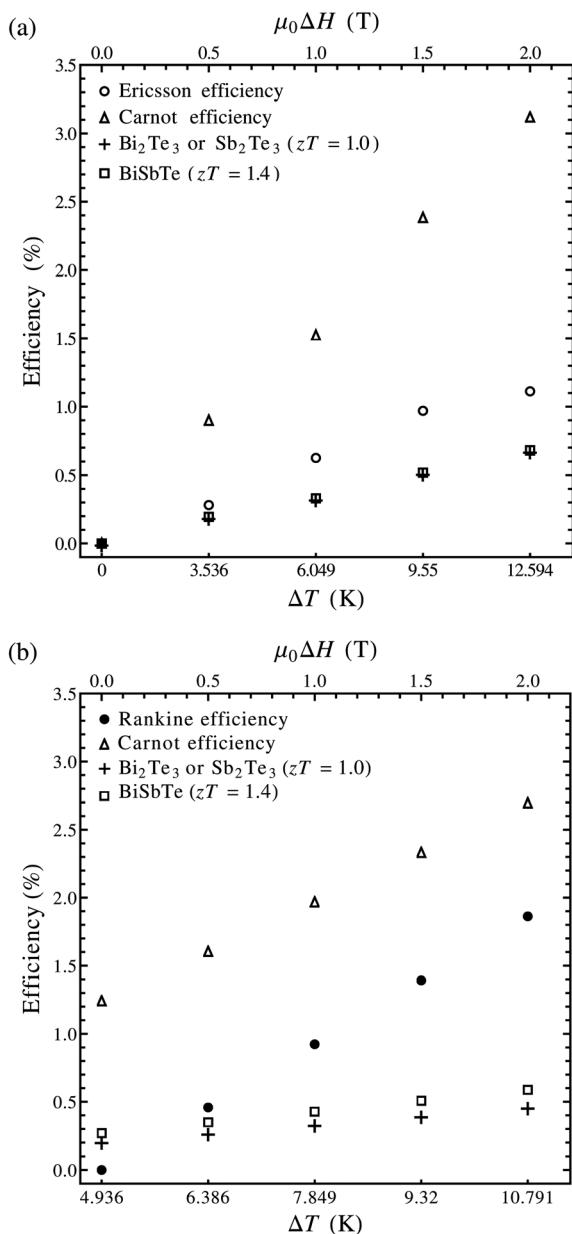
$$\eta_{te} = \left(1 - \frac{T_{min}}{T_{max}}\right) \frac{\sqrt{1 + z\overline{T}} - 1}{\sqrt{1 + z\overline{T}} + T_{min}/T_{max}}, \tag{16}$$

where $\overline{T} = (T_{min} + T_{max})/2$, and $zT = \sigma S^2/\kappa$ is the figure of merit of the material at temperature T. Here, S is the temperature-dependent Seebeck coefficient, σ is the electrical conductivity, and κ is the thermal conductivity. Here it is important to note that for thermoelectrics there are two figures of merit in common use, zT and ZT. The former refers to the material alone, as can be seen from its definition, while the latter is for the whole device: for whole devices, ZT is in fact typically calculated from eqn (16) (with of course zT replaced by ZT) and the measured efficiency of the device (see, e.g., Snyder and Toberer,[29] p. 112, box 4).

Since our predictions above refer to material rather than device, we compare the efficiency of energy conversion of aforementioned cycles with the thermoelectric efficiency η_{te} based on the material figure of merit zT and the working temperature near the transformation temperature of $Ni_{44}Co_6Mn_{40}Sn_{10}$. The best currently available thermoelectric materials at $\overline{T} = 140\,°C$ have $zT \approx 1$ (n-type Bi_2Te_3 paired with p-type Sb_2Te_3). In 2008, a hot pressed nanocrystalline powder of BiSbTe having $zT = 1.4$ near $100\,°C$ was reported.[30] Below we use both $zT = 1.0$ and $zT = 1.4$ in our comparisons.

We compare the efficiency of thermomagnetic Ericsson, Rankine and Carnot cycles with that of a thermoelectric having the figure of merit $zT = 1.0$, 1.4 in Fig. 9. The thermomagnetic cycles are all assumed to be working at the temperature difference given by the difference between two fields, ΔH, in Fig. 9. The efficiency of thermomagnetic Ericsson cycles are computed without assuming regeneration, as then they recover the Carnot efficiency. Excluding thermoelectric generators using radioisotopes, commercial thermoelectric generators generally operate in the range under $\Delta T = 100$ K. For these, the comparison in Fig. 9 shows a competitive efficiency by this new energy conversion method.

1322 | *Energy Environ. Sci.*, 2013, **6**, 1315–1327

This journal is © The Royal Society of Chemistry 2013

(a)

(b)

Fig. 9 Efficiencies of thermodynamic cycles. The efficiencies of thermomagnetic Ericsson (a) and Rankine (b) cycles are compared with the Carnot efficiency and that of conventional thermoelectric devices with $zT = 1.0$ and 1.4 at the given temperature differences that are related to ΔH as described in the captions of Fig. 8 and 7.

According to the aforementioned discussion on the Clausius–Clapeyron relation, the strategy of improving material properties here is to lower the ratio between latent heat and zero-field transformation temperature while retaining a large change in magnetization.
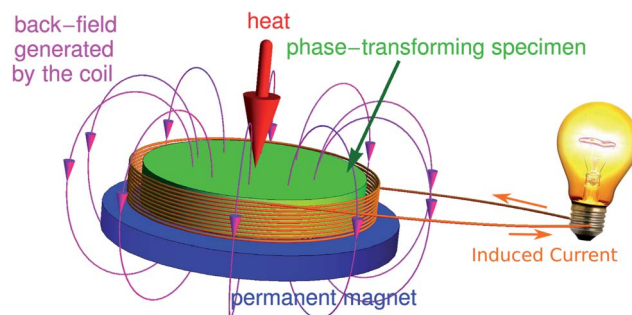
6 Energy conversion

The comparison summarized in Fig. 9 concerns the efficiency of materials only, both for the thermoelectric and multiferroic devices, with the electromagnetic work output calculated using standard definitions, but not accounting for the way the work output is recovered. Here we postulate and analyze a specific mechanism.

In this section we consider an axisymmetric specimen of the working material surrounded by a pick-up coil and placed near a permanent magnet which applies a background field. The coil is connected to a load that is modeled by a resistor here. We heat and cool the specimen by forced convection or radiation. During the phase transformation, the change in magnetization generates a current in the pick-up coil due to Faraday's law, and this coil further induces a *back-field* on the core region. This back-field decreases (resp., increases) the external field during heating (resp., cooling). Thus the efficiency of converting heat into magnetic work can be estimated by a thermomagnetic Ericsson or Rankine cycle as discussed in the previous section with the change of the field due to the changing back-field. It is the goal of this section to analyze how much of this magnetic work is recovered as the electric work on the load by the proposed device. A schematic of the device is shown in Fig. 10.

In this section we use H to denote the total magnetic field including external (H_{ext}) and self-induced (H_m) parts, where the external field further splits into two parts: an applied field (H_0) and a current-induced back field (H_b). The magnetic power done by the external field on the specimen is

$$\mathscr{P}_{mag} = \int_{\Omega} \mu_0 H_{ext} \cdot \dot{M} \mathrm{d}x. \tag{17}$$

We model the permanent magnet as a fixed background field $B_0 = \mu_0 H_0$ distributed uniformly over Ω. If the thermodynamic system is chosen to be the specimen alone, the first law of thermodynamics gives

Another noteworthy feature of the efficiency, especially for thermomagnetic Rankine cycles, is that as ΔH increases, the efficiency increases. What's more, for a Rankine cycle, the efficiency approaches to the Carnot efficiency as ΔH increases. However, a ΔH larger than 2 T is impractical in most cases. An alternative strategy is to use a material with a strong effect of field on transformation temperature, so that the same ΔH corresponds to a larger ΔT, and therefore provides a higher efficiency. Geometrically, in Fig. 9, such a material would move the curves corresponding to thermomagnetic Rankine and Ericsson cycles to the left, while keeping all other curves fixed.

Fig. 10 A schematic view of the proposed device.

$$\frac{\mathrm{d}}{\mathrm{d}t} \int_{\Omega} u \mathrm{d}\boldsymbol{x} = -\oint_{\partial\Omega} \boldsymbol{q}\cdot\boldsymbol{n}\mathrm{d}a + \int_{\Omega} \mu_0(\boldsymbol{H}_0 + \boldsymbol{H}_b)\cdot\dot{\boldsymbol{M}}\mathrm{d}\boldsymbol{x}, \qquad (18)$$

where u is the internal energy density, $\boldsymbol{q}$ is the heat flux per unit area, and $\boldsymbol{n}$ is the outer normal of the surface $\partial\Omega$. The left hand side of eqn (18) is the rate of change of the total internal energy. The first term on the right hand side is the total heat flux flowing across the boundary of Ω. The second term on the right hand side is the magnetic power done by the external field on the specimen, as noted above. In this case, the external field contains both the background field from the permanent magnet, $\boldsymbol{H}_0$, and the back-field induced by the coil, $\boldsymbol{H}_b$. Define the total internal energy U and heating power $\mathscr{Q}$ by

$$U = \int_{\Omega} u \mathrm{d}\boldsymbol{x}, \quad \mathscr{Q} = -\oint_{\partial\Omega} \boldsymbol{q}\cdot\boldsymbol{n}\mathrm{d}a. \qquad (19)$$

The integration of the first law around a closed cycle therefore gives

$$\int_{\mathscr{C}} \mathscr{Q}\mathrm{d}t = -\int_{\mathscr{C}}\int_{\Omega} \mu_0\boldsymbol{H}_b\cdot\dot{\boldsymbol{M}}\mathrm{d}\boldsymbol{x}\mathrm{d}t, \qquad (20)$$

where $\mathscr{C} = [0, t_1]$ is the time interval of the cycle. Since no internal dissipation is considered, the integral on the left hand side $(= \int_{\mathscr{C}} T\dot{S}\mathrm{d}t)$ is the area of the corresponding loop in the T–S diagram discussed in the previous section. Here we have shown that the net heat is converted into magnetic work done by the back-field on the specimen. Next, we show that this magnetic work equals the electric work on the load, $\int_{\mathscr{C}} I^2 R\mathrm{d}T$, where I is the current in the coil and R is the resistance of the load. The proof can take two approaches: one is a direct proof by Maxwell's equations, and the other is by rewriting the first law for a different choice of the system that consists of all the components, *i.e.* specimen, permanent magnet, coil and load resistor.

In the second approach in which the system consists of the specimen, permanent magnet, coil and resistor, we have to model the continuous cooling of the resistor which is necessary to restore the system to its original state after each cycle. (Of course, in applications, this dissipation to heat would occur in the extended systems served by the energy conversion device.) Without loss of generality, we choose the boundary of this system large enough so that no fields cross it. Since no work is done by this system and there is no change of internal energy in a full cycle, it is then seen that the first law for this system is the heat balance,

$$\int_{\mathscr{C}} \mathscr{Q}\mathrm{d}t = \int_{\mathscr{C}} I^2 R\mathrm{d}t, \qquad (21)$$

i.e., the heat absorbed of the specimen equals the heat dissipated by the load.

Combining eqn (21) with (20) we get

$$-\int_{\mathscr{C}}\int_{\Omega} \mu_0\boldsymbol{H}_b\cdot\dot{\boldsymbol{M}}\mathrm{d}\boldsymbol{x}\mathrm{d}t = \int_{\mathscr{C}} I^2 R\mathrm{d}t. \qquad (22)$$

Eqn (22) says that the thermomagnetic efficiency calculated in the previous section is the same as the efficiency of converting heat into electricity using the proposed device, under the assumptions made here. Hence, we conclude that *the magnetic work done by the specimen is fully recovered to the electric work on the load*. In other words, in the formula $\eta = W/Q^+$ used for efficiency in the Section 4, W is equal to the electric energy dissipated in the load resistor. This argument also clarifies the important role of the back-field in producing this work.

To solve either version of the first law of thermodynamics for the power output, we need relationships among $\dot{\boldsymbol{M}}$, $\boldsymbol{H}_b$ and I. These relationships are affected by micromagnetic phenomena, heat transfer properties of the heating device and specimen, and the kinetics of phase transformation. A more device-oriented analysis, in addition to a 3D kinetic model of the phase-changing material, is required to further evaluate the performance of such devices.

The final remark we want to make is about demagnetization. Demagnetization is expected to introduce a strong shape dependence to the energy landscape of the material (see Appendix). In the energy conversion system proposed in this section, although the total magnetic work done by the demagnetization field, $\int_{\mathscr{C}}\boldsymbol{H}_m\cdot\dot{\boldsymbol{M}}\mathrm{d}t$, in a full cycle vanishes, as noted above, it still plays an important role on the specimen-shape dependence of total (magnetic or electric) work output through its influence on the back field. It can be seen by the following arguments. Ampère's law gives a linear relation between the back-field and the current in the coil, $\boldsymbol{H}_b \propto I$. Faraday's law gives a linear relation between the current and the rate of change in magnetic flux, $I \propto \dot{\boldsymbol{B}}$. Thus, we have $\boldsymbol{H}_b \propto \dot{\boldsymbol{B}}$. The primary contribution to $\dot{\boldsymbol{B}}$ is the abrupt change in magnetization across phase transformation. Due to demagnetization, this contribution has two components: $\dot{\boldsymbol{H}}_m$ and $\dot{\boldsymbol{M}}$. $\boldsymbol{H}_m$ is in general proportional to $\boldsymbol{M}$. Thus, a significant demagnetization field kills part of the change in magnetization and therefore reduces $\dot{\boldsymbol{B}}$ drastically, which in turn lowers the back-field $\boldsymbol{H}_m$, shrinks the thermomagnetic cycle in the T–S diagram, and finally reduces the efficiency. However, demagnetization is not the only shape-dependent factor in this kind of devices, other such factors include the heat transfer property. A comprehensive analysis on the shape-dependence of the efficiency and the power output, again, requires a more sophisticated thermodynamic model.

7 Conclusions

Temperature and field induced first order phase transformations are investigated in the alloy $Ni_{44}Co_6Mn_{40}Sn_{10}$. The properties are found to be suitable for the heat to electricity energy conversion technology recently discovered by Srivastava *et al.* in ref. 2. A thermodynamic theory aiming at analyzing the energy conversion utilized by these new materials is developed. We summarize our main conclusions:

1. A simple Gibbs free energy function as a function of external magnetic field and temperature T is determined from calorimetric and magnetic measurements on this alloy, using a simple version of molecular field theory. This function reproduces well the temperature and field-induced phase transformations and the effect of field on transformation

1324 | *Energy Environ. Sci.*, 2013, **6**, 1315–1327

This journal is © The Royal Society of Chemistry 2013

temperature. This free energy has a precise relation to 3D models that account for magnetic domains, phase transformation, deformation, elasticity and microstructure. This relation reveals that M is the volume average magnetization (averaged over the deformed configuration), and that the simple free energy includes the contribution from the demagnetization energy. The latter can be estimated from the 3D theory.

2. The entropy as a function of field and temperature is obtained from the Gibbs energy. We show that this thermodynamic model admits thermomagnetic Carnot, Ericsson and Rankine cycles with relatively large area in the mixed phase region. These are conveniently represented on the T–S diagram, as in the classical case. Efficiency is computed for these cycles and compared with the Carnot efficiency and that of thermoelectrics. The result shows that the method of thermomagnetic energy conversion investigated here is competitive with the best available thermoelectric materials. Furthermore, materials with a strong effect of magnetic field on transformation temperature are desirable for this method.

3. A proposed device utilizing induction and a biasing magnet is used to connect the aforementioned thermomagnetic cycles of a material to the electric work output of the device using this method of energy conversion. As a result, we found that in the proposed design, the net magnetic work done by the specimen is fully converted into electricity. A more accurate estimation on the power output requires extending the quasi-static thermodynamics to that for finite-rate processes, which will be included in future work.

8 Appendix: magnetism and phase transformation

In this paper we determine from measurements a simple free energy (density) of the form $\varphi(M, T)$ as a function of a scalar magnetization M and temperature T. In this section we explain how the simple free energy used in this paper is related to more sophisticated models that account for more features of an actual polycrystal specimen such as highly nonuniform vector magnetization due to the presence of magnetic domains and complex distortions in the martensite phase including twinning and approximate interfaces between martensite plates.

Let Ω be the region occupied by the specimen in the undistorted austenite phase at T_0. Deformations of Ω due to both elastic distortion and transformation are described by a deformation vector field $\boldsymbol{y}(\boldsymbol{x})$, $\boldsymbol{x} \in \Omega$ giving the new position $\boldsymbol{y}$ of the particle originally located at $\boldsymbol{x}$. The magnetization vector field, $\boldsymbol{M}(\boldsymbol{y})$, is defined on the deformed configuration $\boldsymbol{y}(\Omega)$. A free energy functional that accounts for complex magnetization and phase transformation is[31–33]

$$E[\boldsymbol{y}, \boldsymbol{M}] = \int_\Omega \Big\{ A|\nabla \boldsymbol{M}|^2 + W(\nabla \boldsymbol{y}(\boldsymbol{x}), \boldsymbol{M}(\boldsymbol{y}(\boldsymbol{x})), T) $$
$$- \boldsymbol{B}_{\text{ext}} \cdot \boldsymbol{M}(\boldsymbol{y}(\boldsymbol{x})) \det \nabla \boldsymbol{y}(\boldsymbol{x}) \Big\} \mathrm{d}x + \frac{\mu_0}{2} \int_{\mathbb{R}^3} |\nabla u|^2 \mathrm{d}\boldsymbol{y}, \quad (23)$$

where μ_0 is the vacuum permeability, and A is the exchange constant. The magnetostatic potential u depends uniquely

(up to an additive constant) on the magnetization, and is obtained by solving the magnetostatic equation,

$$\nabla(-\nabla u + \boldsymbol{M}) = 0, \quad (24)$$

on all of space for a trial magnetization $\boldsymbol{M}(\boldsymbol{y})$, which is assumed to vanish outside of $\boldsymbol{y}(\Omega)$. The first term on the right hand side of eqn (23) is a simple form of the exchange energy. The second term is the multi-well bulk free energy density and includes anisotropy energy, elastic energy, and free energy differences between phases. The third term is the Zeeman energy corresponding to the external magnetic field $\boldsymbol{B}_{\text{ext}} = \mu_0 \boldsymbol{H}_{\text{ext}}$, which can alternatively be written in the more conventional form

$$-\mu_0 \int_{\boldsymbol{y}(\Omega)} \boldsymbol{H}_{\text{ext}} \cdot \boldsymbol{M}(\boldsymbol{y}) \mathrm{d}\boldsymbol{y}. \quad (25)$$

The phase transformation is modeled by the symmetries and the energy-well structure of W. In general, W is Galilean invariant and exhibits the symmetries implied by an appropriate form of the Cauchy–Born rule[34,35] combined with the Ericksen–Pitteri neighborhood.[35,36] In the case of $Ni_{44}Co_6Mn_{40}Sn_{10}$ in which only the austenite is ferromagnetic, this leads to the energy-well structure of the following type:

$$W(\boldsymbol{I}, \boldsymbol{M}_1, T) = \ldots = W(\boldsymbol{I}, \boldsymbol{M}_r, T) \leq W(\boldsymbol{F}, \boldsymbol{M}, T) \text{ for } T > T_0; \quad (26)$$

$$W(\boldsymbol{U}_1, 0, T) = \ldots = W(\boldsymbol{U}_{12}, 0, T) \leq W(\boldsymbol{F}, \boldsymbol{M}, T) \text{ for } T \leq T_0, \quad (27)$$

where $\boldsymbol{U}_n$, $n = 1, \ldots, 12$, is the right Green stretch tensor of the deformation from undistorted austenite to the nth undistorted martensite variant. These inequalities are required to hold for all $(\boldsymbol{F}, \boldsymbol{M}, T)$ in the domain of W, where $\boldsymbol{F}$ is the 3-by-3 matrix representing the deformation gradient $\nabla \boldsymbol{y}$. The first inequality says that when $T > T_0$, W is *equally* minimized by the austenite lattice with the magnetization pointing in the special directions, $\boldsymbol{M}_1, \ldots, \boldsymbol{M}_r$. These special directions are determined by the point group of austenite lattice. The second inequality says that when $T \leq T_0$, W is equally minimized by 12 martensite variants with zero magnetization. The forms of the twelve tensors $\boldsymbol{U}_1, \ldots, \boldsymbol{U}_{12}$ are restricted by the point groups of austenite and martensite. In the orthonormal cubic basis, $\boldsymbol{U}_1$ of $Ni_{45}Co_5Mn_{40}Sn_{10}$ is obtained from X-ray data,[1]

$$\boldsymbol{U}_1 = \begin{pmatrix} 1.0054 & 0.0082 & 0 \\ 0.0082 & 1.0590 & 0 \\ 0 & 0 & 0.9425 \end{pmatrix}, \quad (28)$$

with ordered eigenvalues $(\lambda_1, \lambda_2, \lambda_3) = (0.9425, 1.0042, 1.0602)$. In particular, as noted in the introduction section, $\lambda_2 = 1.0042$.

Let angled brackets denote the volume average over the deformed configuration $\boldsymbol{y}(\Omega)$ and $\mathscr{V}_y = \text{vol.}(\boldsymbol{y}(\Omega))$:

$$\langle \boldsymbol{M} \rangle_{\boldsymbol{y}(\Omega)} = \frac{1}{\mathscr{V}_y} \int_{\boldsymbol{y}(\Omega)} \boldsymbol{M}(\boldsymbol{y}) \mathrm{d}\boldsymbol{y}. \quad (29)$$

The simple Helmholtz free energy $\varphi(M, T)$ is obtained from the general free energy functional $E[\boldsymbol{y}, \boldsymbol{M}]$ by constrained minimization, but excluding the Zeeman energy,

This journal is © The Royal Society of Chemistry 2013

Energy Environ. Sci., 2013, **6**, 1315–1327 | **1325**

$$\varphi(M, T) = \min_{|\langle M \rangle_{y(\Omega)}| = M} \frac{1}{\mathscr{V}_y} \left(\int_\Omega A|\nabla M|^2 \right.$$

$$\left. + W(\nabla y(x), M(y(x)), T) \, dx + \frac{\mu_0}{2} \int_{\mathbb{R}^3} |\nabla u|^2 dy \right). \tag{30}$$

With appropriate function spaces for y, M, and suitable mild growth conditions on $W(F, M, T)$ for large F, the minimum (or, at least the infimum) of the term in parentheses exists, so this constrained minimization is well-posed.

Now we read off properties of φ from this definition. First, we see that M should be interpreted as the magnitude of the energy minimizing volume-averaged magnetization, averaged over the deformed configuration. Second, if the Zeeman energy with a *uniform* external field is added, then the appropriate general minimization is

$$\min E[y, M] = \min_M \left(\min_{|\langle M \rangle_{y(\Omega)}| = M} E[y, M] \right)$$

$$= \min_M (\varphi(M, T) - \mu_0 H_{\text{ext}} M), \tag{31}$$

where H_{ext} is the component of $\boldsymbol{H}_{\text{ext}}$ along the average minimizing magnetization. Note that the latter simplification relies in an important way on having a uniform external field. Eqn (31) justifies the minimization problem used below to partly determine $\varphi(M, T)$. Third, it is seen from the definition of $\varphi(M, T)$ that demagnetization energy (the last term of eqn (30)) is included in $\varphi(M, T)$. This is important, as it implies that changing the shape of the specimen but keeping the material the same will result in a different $\varphi(M, T)$. In the main part of this paper, all measurements used to evaluate $\varphi(M, T)$ were done on the same specimen or are shape-independent. This specimen contained small surface cracks that could affect the demagnetization energy, so we have not tried to separate out this contribution to φ.

However, it is useful to estimate the influence of demagnetization energy. We note that there is a rigorous lower bound for the contribution of the demagnetization energy to $\varphi(M, T)$ in the case that the deformed configuration is an ellipsoid. That is, if $y(\Omega)$ is an ellipsoid, then the constrained minimization of the demagnetization energy alone has an explicit solution:

$$\min_{|\langle M \rangle_{y(\Omega)}| = M} \left(\frac{\mu_0}{2\mathscr{V}_y} \int_{\mathbb{R}^3} |\nabla u|^2 dy \right) = \frac{\mu_0}{2} \min_{|m| = M} \boldsymbol{m} \cdot \boldsymbol{Dm}, \tag{32}$$

where $\boldsymbol{D}$ is the demagnetization matrix of the ellipsoid (see, *e.g.*, Lemma A.1 in ref. 37). The meaning of the minimization problem on the left hand side of eqn (32) is the following: (i) given M, a trial magnetization $\boldsymbol{M}(y)$ is chosen satisfying the constraint $|\langle M \rangle_{y(\Omega)}| = M$, (ii) the magnetostatic equation, eqn (24), is solved for the corresponding potential $u(y)$, (iii) the demagnetization energy of u is calculated from the integral in eqn (32), (iv) the trial magnetization giving the lowest value of the demagnetization energy is found. A simple final lower bound for the right hand side of eqn (32) is $\mu_0/2$ times the minimum eigenvalue of the demagnetization matrix, but a better bound can be given if information about the direction of the minimizing average magnetization is known. Now using the general inequality $\min(A + B) \geq \min A + \min B$ and the bound eqn (32) we deduce from eqn (30) that

$$\varphi(M, T) \geq \hat{\varphi}(M, T) + \frac{\mu_0}{2} \min_{|m| = M} \boldsymbol{m} \cdot \boldsymbol{Dm}, \tag{33}$$

where $\hat{\varphi}(M, T)$ is the constrained minimum free energy with demagnetization energy excluded, *i.e.*, $\hat{\varphi}(M, T)$ is shape-independent. This lower bound is expected to be a good estimate based on results given in ref. 37, for example, if the magnetization varies on a fine scale but is macroscopically nearly constant. Overall, it is seen from this bound that demagnetization energy can be an important contribution to the total free energy that is expected to play a role in carefully designed energy conversion devices.

In summary, $\varphi(M, T)$ relates precisely by constrained minimization to 3D models of micromagnetics and phase transformation. M is interpreted as the volume averaged magnetization over the deformed configuration. Under the important condition that the external field is uniform and the average magnetization points in the direction of the external field, there is the implied minimization problem $\min_M(\varphi(M, T) - \mu_0 H_{\text{ext}} M)$. Finally, $\varphi(M, T)$ includes demagnetization effects but these can be estimated if the deformed configuration is approximately ellipsoidal.

The minimum value of the right hand side of eqn (31) is the Gibbs free energy as a function of external field and temperature

$$\psi(H_{\text{ext}}, T) = \min_M (\varphi(M, T) - \mu_0 H_{\text{ext}} M). \tag{34}$$

The Gibbs free energy ψ is easier to fit from experimental data than the multiwell (Helmholtz) free energy φ, but care must be taken to fit it only from single phase data, where the inversion allowing passage from ψ back to φ is valid. Or, from a physical viewpoint, given values of H_{ext}, T can correspond to mixed phase states. For the simplicity of notation, we denote the external magnetic field by H instead of H_{ext} in the main part of this paper, unless otherwise mentioned.

Acknowledgements

References

1 V. Srivastava, X. Chen and R. D. James, *Appl. Phys. Lett.*, 2010, **97**, 014101.

1326 | *Energy Environ. Sci.*, 2013, **6**, 1315–1327

This journal is © The Royal Society of Chemistry 2013

2 V. Srivastava, Y. Song, K. Bhatti and R. D. James, *Adv. Energy Mater.*, 2011, **1**, 97.

3 R. D. James and Z. Zhang, *The Interplay of Magnetism and Structure in Functional Materials*, New York, 2005, p. 159.

4 K. P. Bhatti, S. El-Khatib, V. Srivastava, R. D. James and C. Leighton, *Phys. Rev. B: Condens. Matter Mater. Phys.*, 2012, **85**, 134450.

5 Y. Sutou, Y. Imano, N. Koeda, T. Omori, R. Kainuma, K. Ishida and K. Oikawa, *Appl. Phys. Lett.*, 2004, **85**, 4358–4360.

6 R. Kainuma, Y. Imano, W. Ito, H. Morito, Y. Sutou, K. Oikawa, A. Fujita, K. Ishida, S. Okamoto, O. Kitakami and T. Kanomata, *Appl. Phys. Lett.*, 2006, **88**, 192513.

7 R. Kainuma, Y. Imano, W. Ito, Y. Sutou, H. Morito, S. Okamoto, O. Kitakami, K. Oikawa, A. Fujita, T. Kanomata and K. Ishida, *Nature*, 2006, **439**, 957–960.

8 T. Krenke, E. Duman, M. Acet, E. F. Wassermann, X. Moya, L. Manosa and A. Planes, *Nat. Mater.*, 2005, **4**, 450–454.

9 S. Y. Yu, L. Ma, G. D. Liu, Z. H. Liu, J. L. Chen, Z. X. Cao, G. H. Wu, B. Zhang and X. X. Zhang, *Appl. Phys. Lett.*, 2007, **90**, 242501–242503.

10 H. E. Karaca, I. Karaman, B. Basaran, Y. Ren, Y. I. Chumlyakov and H. J. Maier, *Adv. Funct. Mater.*, 2009, **19**, 983–998.

11 K. Bhattacharya, *Microstructure of martensite: why it forms and how it gives rise to the shape-memory effect*, Oxford University Press, Oxford, 2003.

12 Z. Zhang, R. D. James and S. Müller, *Acta Mater.*, 2009, **57**, 4332–4352.

13 R. Delville, S. Kasinathan, Z. Zhang, J. V. Humbeeck, R. D. James and D. Schryvers, *Philos. Mag.*, 2010, **90**, 177–195.

14 R. Zarnetta, R. Takahashi, M. L. Young, A. Savan, Y. Furuya, S. Thienhaus, B. Maaß, M. Rahim, J. Frenzel, H. Brunken, Y. S. Chu, V. Srivastava, R. D. James, I. Takeuchi, G. Eggeler and A. Ludwig, *Adv. Funct. Mater.*, 2010, **20**, 1917–1923.

15 X. Chen, V. Srivastava and R. D. James, J. Mech. Phys. Solids, 2013, submitted.

16 J. Glanz, *Science*, 1998, **78**, 2045.

17 V. K. Pecharsky and K. A. Gschneidner, Jr, *J. Magn. Magn. Mater.*, 1997, **200**, 44–56.

18 V. K. Pecharsky and K. A. Gschneidner, Jr, *Phys. Rev. Lett.*, 1997, **78**, 4497–4497.

19 V. K. Pecharsky, *J. Magn. Magn. Mater.*, 1997, **167**, L179.

20 O. Tegus, E. Brcka, L. Zhanga, Dagulaa, K. H. J. Buschowa and F. R. de Boera, *Phys. B*, 2002, **319**, 174–192.

21 S. Nikitin, G. Myalikgulyev, A. M. Tishina, M. P. Annaorazov, K. A. Asatryan and A. L. Tyurin, *Phys. Lett. A*, 1990, **148**, 363–366.

22 V. Provenzano, A. J. Shapiro and R. D. Shull, *Nature*, 2004, **429**, 853–857.

23 S. Maat, J. U. Thiele and E. E. Fullerton, *Phys. Rev. B: Condens. Matter Mater. Phys.*, 2005, **72**, 214432.

24 V. Sokolovskiy, V. Buchelnikov, M. Zagrebin, P. Entel, S. Sahool and M. Ogura, *Phys. Rev. B: Condens. Matter Mater. Phys.*, 2012, **86**, 1–11.

25 D. O. Smith, *Phys. Rev.*, 1956, **102**, 959–963.

26 J. Cui, Y. S. Chu, O. O. Famodu, Y. Furuya, J. Hattrick-Simpers, R. D. James, A. Ludwig, S. Thienhaus, M. Wuttig, Z. Zhang and I. Takeuchi, *Nat. Mater.*, 2006, **5**, 286–290.

27 S. Fujino, M. Murakami, V. Anbusathaiah, S.-H. Lim, V. Nagarajan, C. J. Fennie, M. Wuttig, L. Salamanca-Riba and I. Takeuchi, *Appl. Phys. Lett.*, 2008, **92**, 202904.

28 G. J. Snyder and T. S. Ursell, *Phys. Rev. Lett.*, 2003, **91**, 148301.

29 G. J. Snyder and E. S. Toberer, *Nat. Mater.*, 2008, **7**, 105–114.

30 B. Poudel, Q. Hao, Y. Ma, Y. Lan, A. Minnich, B. Yu, X. Yan, D. Wang, A. Muto, D. Vashaee, X. Chen, J. Liu, M. S. Dresselhaus, G. Chen and Z. Ren, *Science*, 2008, **320**, 634–638.

31 R. James and D. Kinderlehrer, *Philos. Mag. B*, 1993, **68**, 237–274.

32 R. D. James and K. F. Hane, *Acta Mater.*, 2000, **48**, 197–222.

33 W. Brown, *Magnetoelastic Interactions*, Springer-Verlag, Berlin, Heidelberg, 1966, vol. 9.

34 J. L. Ericksen, in *Phase Transformations and Material Instabilities in Solids*, ed. M. E. Gurtin, Academic, New York, 1984, pp. 61–77.

35 M. Pitteri and G. Zanzotto, *Continuum models for phase transitions and twinning in crystals*, Chapman and Hall/CRC, Boca Raton, Florida, 2002, vol. 9.

36 J. L. Ericksen, *Arch. Ration. Mech. Anal.*, 1980, **73**, 99–124.

37 A. DeSimone and R. D. James, *J. Mech. Phys. Solids*, 2002, **50**, 283–320.